nature communications

Article

https://doi.org/10.1038/s41467-024-54510-9

Coacervate-pore complexes for selective molecular transport and dynamic reconfiguration

Received: 10 April 2024

Accepted: 13 November 2024

Published online: 20 November 2024

Check for updates

Hao Wang[1,2,3], Hui Zhuang[4], Wenjing Tang[5], Jun Zhu[1,2,3], Wei Zhu[5] ✉ & Lingxiang Jiang[1,2,3] ✉

Despite surging interests on liquid-state coacervates and condensates, confinement within solid-state pores for selective permeation remains an unexplored area. Drawing inspiration from nuclear pore complexes (NPCs), we design and construct coacervate-pore complexes (CPCs) with regulatable permeability. We demonstrate universal CPC formation across 19 coacervate systems and 5 pore types, where capillarity drives the spontaneous imbibition of coacervate droplets into dispersed or interconnected pores. CPCs regulate through-pore transport by forming a fluidic network that modulates guest molecule permeability based on guest-coacervate affinity, mimicking NPC selectivity. While solid constructs of NPC mimicries are limited by spatial fixation of polymer chains, CPCs of a liquid nature feature dynamic healing and rapid phase transitioning for permeability recovery and regulation, respectively. Looking forward, we expect the current work to establish a basis for developing liquid-based NPC analogs using a large pool of synthetic coacervates and biomolecular condensates.

Nuclear pore complexes (NPCs) are evolutionarily advanced, gigantic molecular machinery perforating the nuclear envelope to connect the nucleus and cytoplasm for a dedicated purpose—controlling the nucleocytoplasmic traffic[1,2]. They reject or suppress the transport of most macromolecules while grant rapid translocation of small molecules and large nuclear transport receptors (NTRs). NTRs in turn can efficiently shuttle macromolecular cargoes between the two physically separated compartments. Structurally, NPCs are sophisticated supramolecular organizations of multiple copies of ~30 different proteins (total mass >10^8 Da, Fig. 1a), featuring a ~40-nm wide central channel that critically act as a selective permeability barrier[3,4]. In this channel are tethered disordered proteins rich in FG (Phe-Gly) repeats that form a network reversibly crosslinked by the cohesive, multivalent inter-FG interactions[5,6]. It is an ongoing endeavor in chemistry and materials science to develop artificial systems that can reproduce and ultimately surpass the native NPCs in terms of selective permeation and facilitated transportation[7,8]. Two synthetic constructs based on grafted brushes and crosslinked gels, respectively, have been extensively studied. In the first construct, polymer brushes of FG-rich proteins or synthetic polymers are grafted onto solid-state pores to repel inert macromolecules by volume exclusion and to allow the passage of NTRs or synthetic carriers due to brush-carrier affinity (Fig. 1b)[9–12]. In the second construct, a gel network of FG-rich proteins operates as a molecular sieve that rejects inert macromolecules yet favors the flux of

[1]South China Advanced Institute for Soft Matter Science and Technology (AISMST), School of Emergent Soft Matter, South China University of Technology, Guangzhou 510640, China. [2]Guangdong Provincial Key Laboratory of Functional and Intelligent Hybrid Materials and Devices, Guangdong Basic Research Center of Excellence for Energy & Information Polymer Materials, South China University of Technology, Guangzhou 510640, China. [3]State Key Laboratory of Pulp and Paper Engineering, South China University of Technology, Guangzhou 510640, China. [4]Experimental Basis and Practical Training Center, South China Agricultural University, Guangzhou 510642, China. [5]MOE International Joint Research Laboratory on Synthetic Biology and Medicines, School of Biology and Biological Engineering, South China University of Technology, Guangzhou 510006, China. ✉e-mail: zhuwei86@scut.edu.cn; jianglx@scut.edu.cn

https://doi.org/10.1038/s41467-024-54510-9

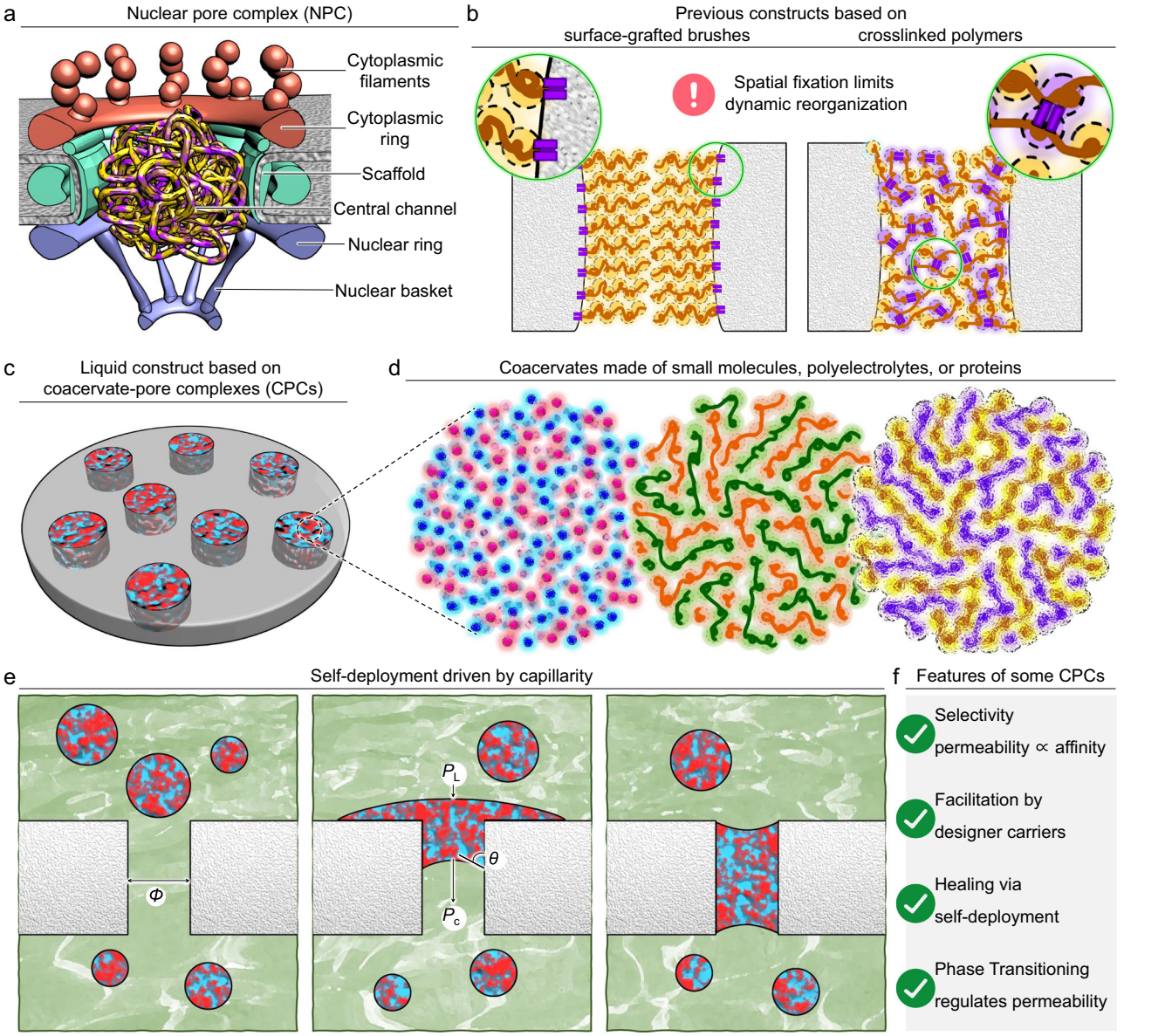

Fig. 1 | Schematic illustrations of nuclear pore complexes (NPCs) and their mimicries of solid or liquid natures. a The molecular machinery of an NPC featuring a central channel filled with FG-rich proteins to act as a molecular sieve. **b** Two solid constructs based on surface-grafted brushes and crosslinked polymers, where the spatial fixations are highlighted by purple staples. **c** A liquid construct based on coacervate-pore complexes (CPCs). **d** The liquid coacervates are made of small molecules (red and blue), polyelectrolytes (orange and green), or proteins (yellow and purple). **e** Inhabitation of coacervate droplets into a pore of diameter (Φ) is a spontaneous process as driven by the capillary pressure (P_c), given that the contact angle (θ) is smaller than 90 °. The Laplace pressure (P_L) has a minor effect. **f** Four features of some CPCs.

NTRs or NTR•cargo complexes (Fig. 1b)[5,13–15]. NTRs can strongly interact with the FG-repeats to effectively disrupt the inter-FG cohesion, enabling themselves to traverse the network with little resistance.

Picture a continuous spectrum from an ideal solid with spatially fixated molecules to an ideal liquid with fully mobile molecules. The gel and brush constructs are soft matter that can be placed between the two limits with increasing molecular dynamics: The whole-chain dynamics is strongly restricted by crosslinkers while segmental dynamics are allowed in the gel construct[13–15], and the polymer chains are subjected to less constrains as only one end is tethered in the brush construct (highlighted by the purple staples in Fig. 1b)[9–12]. There are notable examples of conformational reorganization and dynamic response for gel or brush constructs[16,17]. Intuitively, one would expect faster dynamics, greater reorganization, and stronger response when the in-pore matter is more liquid-like, and we wonder if the dynamics can be pushed to the extreme when a liquid construct is in place.

Synthetic coacervates or biomolecular condensates are liquid droplets of concentrated abiotic or biotic macromolecular solutes, which are held together by multivalent, solute-solute cohesion, in equilibrium with a continuous, dilute phase (Fig. 1d)[18,19]. They are extensively studied in scientific endeavors such as permeable compartmentalization, reaction catalysis, and protocell modeling[20–22], and they are prevalently presented in living cells to perform a wealth of biophysical and biochemical activities such as metabolism, signaling cascades, stress adaptation, and regulation of gene expression[23,24]. Despite the compositional differences, both coacervates and condensates are formed by liquid-liquid phase separation (LLPS) when the homotypic or heterotypic solute-solute attractions outweigh the solute-solvent attractions and the entropic penalty of demixing. We

thus consider them thermodynamically identical and simplify the nomenclatures in this paper by addressing both as coacervates.

Consider now a permeation scenario with a guest molecule and a coacervate phase. The molecularly crowded milieu of a coacervate creates a microenvironment physicochemically different from the dilute phase to favor or disfavor the partitioning of the guest according to the coacervate-guest affinity[25]. The coacervate also imposes a dynamic, polymeric network on the Brownian motion of the guest whose diffusivity depends on the ratio of guest/mesh sizes[26] and the molecular frictions caused by the solvent and the network. The partitioning and diffusivity together may determine the guest permeability in a manner particularly akin to that of the FG-rich gel construct[27], except that the coacervate network is dynamic and fluidic on the experimental timescale. Certain FG-rich proteins and polypeptides were indeed recently discovered to form liquid condensates with NPC-like permeability[28–31], alluding to the feasibility of a coacervate-based construct for NPC mimicry.

Herein, we design and construct coacervate-pore complexes (CPCs) in which solid-state pores are spontaneously filled by liquid coacervates to control the through-pore transportation (Fig. 1c). Specifically, imbibition of coacervate droplets into wettable pores and subsequent firm immobilization are thermodynamically favored, resembling the situation of supported liquid membranes[32,33]. We refer to this capillarity-driven process as self-deployment (Fig. 1e) and observe it for an extensive library of 19 kinds of coacervate systems and 5 kinds of pores. While the solid constructs require complicated assembly or synthesis steps to fixate the pore fillers, the self-deployment of CPCs is universal and effortless. Transportation across a few kinds of CPCs with moderate selectivity is demonstrated by the predominant dependence of guest permeability on the guest-coacervate affinity. Conjugated carriers, analogous to NTRs, are then synthesized to boost the permeation of targeted cargoes. More importantly, we highlight two merits of CPCs' liquid nature—dynamic healing and drastic phase transitioning—which are hardly attainable by the solid constructs (Fig. 1f). When a solid membrane is damaged to create leaky holes or fractures, coacervate droplets can fill the newly perforated openings and restore the permeability. The in-pore coacervates can markedly respond to environmental cues by undergoing transitions to a dissolved or a solid state; correspondingly, CPCs turn from semi-permeable to open or closed states.

Results

Self-deployment of coacervates in solid-state pores

In brief, we freshly prepare a coacervate suspension by mixing two constituent solutions, apply vortex and sonication to produce well-dispersed coacervate droplets, then immerse a porous membrane into this suspension with sonication on for 5 min to load the coacervates into the pores, and finally transfer this membrane of coacervate-pore complexes (CPCs) to a chamber of the dilute phase for further inspections (Fig. 2a). Alternatively, we could load the coacervates into the pores by soaking the porous membrane into a layered coacervate phase. But this approach suffers from the troublesome steps of collecting the coacervate phase in a significant volume and from the extra coacervates adhered to the membrane surface that cannot be easily washed off (Supplementary Fig. 1).

In this section we focus on COA1@POR1, where COA1 denotes the coacervates made of DTAB and PTS (dodecyltrimethylammonium bromide and 1,3,6,8-pyrenetetrasulfonic acid tetrasodium salt, Table 1). DTAB is a surfactant with a cationic headgroup and a hydrophobic tail, PTS is a hydrophobic salt with a pyrene core and 4 anionic side groups (Fig. 3a), and they interact with each other via electrostatic attraction and hydrophobic effect to form coacervate droplets polydisperse in size (Fig. 2b)[19]. POR1 designates the solid-state pores of a cylindrical shape (diameter $\Phi = 3$ μm) on a 9 μm-thick polycarbonate membrane (Table 2). Observations by optical microscopy and scanning electron microscopy (SEM) confirm the pore geometry, their perforation through the membrane, and their sparse distribution on the membrane (Fig. 2c). The as-prepared COA1@POR1 membranes are observed by confocal laser scanning microscopy (CLSM) in a wet condition, where colocalization of pores and fluorescently labeled coacervates verifies the formation of CPCs (Fig. 2e). The 3D reconstruction demonstrates a uniform distribution of coacervates along the length of the cylindrical pores with the pore occupancy approaching 100% (Fig. 2e and Supplementary Fig. 2). This high occupancy is supported by SEM images in a dry condition (Fig. 2d), in which the otherwise empty pores are filled with the solid contents of coacervates (highlighted by arrows).

We dispel a plausible concern that pore confinement may alter the coacervate properties. The unconfined coacervate droplets consist of DTAB, PTS, and water at 40, 24, and 36 wt%, respectively; this composition is retained for in-pore coacervates (Fig. 2g). Fluorescence recovery after photobleaching (FRAP) measurements[34] are performed on the unconfined droplets and in-pore coacervates to probe molecular mobility, where exponential fitting gives diffusivity (D) of a guest dye (Fig. 2h with the sequential recovery images given in the inset). It is demonstrated that the in-pore coacervates are indeed liquid with a D comparable to that of the unconfined droplets (Supplementary Fig. 3). While some biomolecular condensates were reported to undergo solidification or fiberization upon aging[35,36], prolonged observation on in-pore coacervates preclude solidification in the long term (Supplementary Fig. 3). The coacervate-pore interface can therefore be considered as inert boundaries that do not dehydrate the coacervates nor reduce their fluidity in any significant way.

Next we consider the kinetics and thermodynamics of CPC formation. When an empty membrane is immersed in a coacervate suspension, pore filling takes place in two steps[37]. First the volumetrically predominant, dilute phase pushes the trapped air out of the pores by hydrostatic pressure. Then the in-pore dilute phase is gradually displaced by the coacervate phase as coacervate droplets are continually supplied to the pore edges. We reason that the second displacement process is thermodynamically favored, resembling capillary infiltration[37]. Consider a few coacervate droplets in proximity to a cylindrical pore of diameter Φ, both of which are in a bath of the dilute phase (Fig. 1e). When the droplets partially infiltrate the pore, a capillary pressure (P_c) acting on the coacervate/dilute phase interface is given by $P_c = 4\sigma \cos\theta/\Phi$[38], where σ is the interfacial tension between the two liquid phases and θ the contact angle of a coacervate droplet under its dilute phase on the membrane surface. Under a wetting condition of $\theta < 90$ °, P_c will drive the interface towards the dilute phase until complete imbibition, while the Laplace pressure (P_L) on the opposite interface plays a minor role. In the case of COA1@POR1 with $\theta = 38$ ° (preferential wetting by the coacervate phase, Fig. 2f), $\sigma = 0.45$ mN m^{-1}, and $\Phi = 3$ μm, P_c is calculated to be 480 N m^{-2} to strongly drive the imbibition. We thus refer to this spontaneous process as self-deployment, in which sonication merely facilitates it by keeping the droplets afloat and moving around. Control experiments show that the strength of mechanical agitation (high-power sonication or gentle shaking) changes the swiftness of the deployment process but not the final state (Supplementary Fig. 4).

A library of coacervate-pore complexes (CPCs)

Reported coacervate systems are remarkably diverse in constituent chemistry, ranging from abiotic to biological molecules, from small molecules to gigantic biopolymers, from hydrophobic molecules to hydrophilic polysaccharides or polyelectrolytes, and from flexible polymeric chains to rigid nanoparticles[39,40]. This chemical diversity gives rise to disparity in physical properties such as micropolarity, viscosity, and interfacial tension[39,41]. We thus elect 19 representative coacervate systems (denoted as COA1 to COA19, Table 1 and Supplementary Table 1) to cover a significant portion of the chemical space of

https://doi.org/10.1038/s41467-024-54510-9

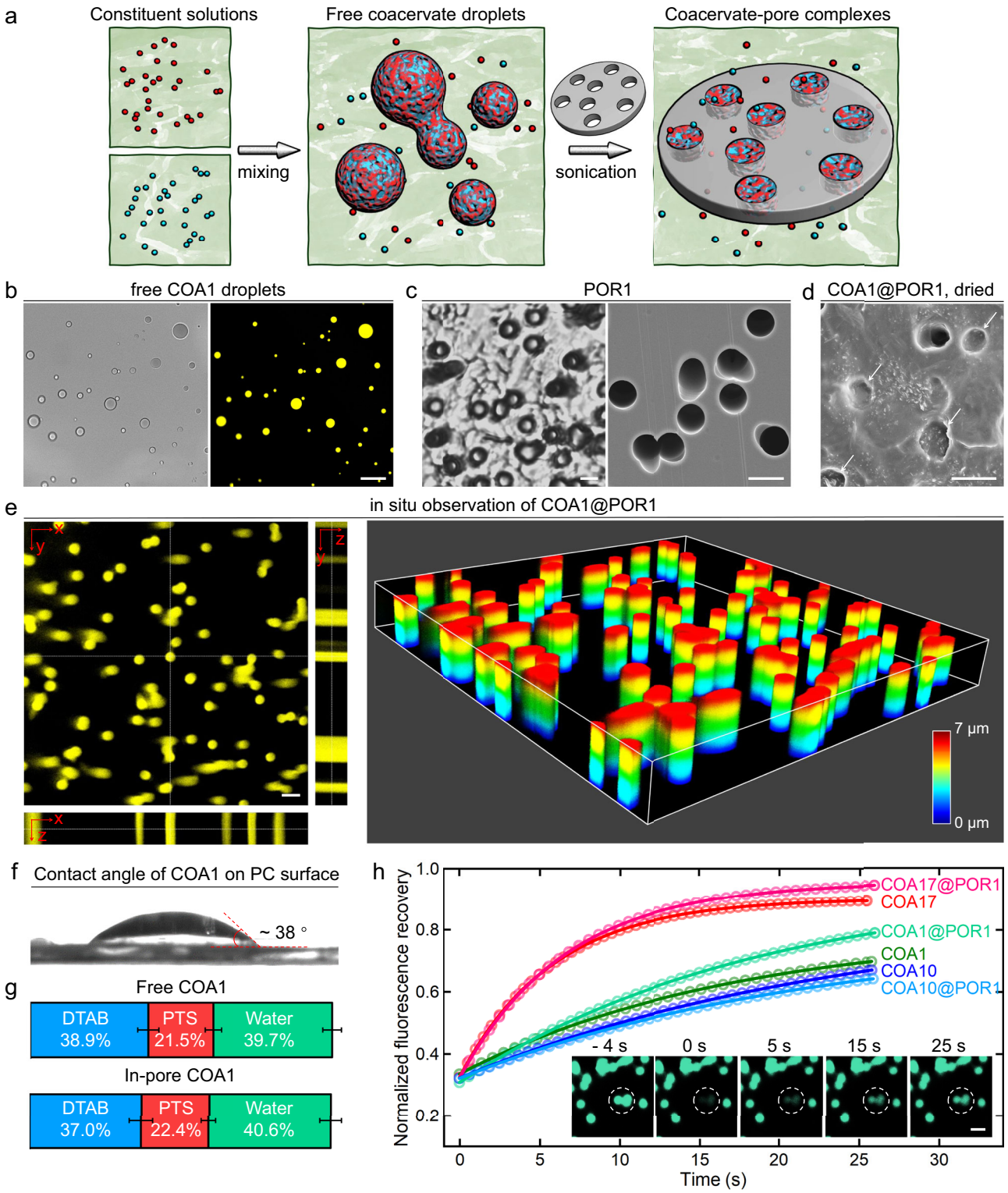

Fig. 2 | The formation and liquidity of coacervate 1/pore 1 complexes (denoted as COA1@POR1). a Self-deployment of coacervate droplets into the solid-state pores. **b** COA1 droplets suspended in the dilute phase as observed in the transmission (left) and fluorescence channel (right). **c** POR1 on PC membranes as imaged by optical microscopy (left) and SEM (right). **d** A SEM picture of dried COA1@POR1 membrane, demonstrating the solid remaining in the pores (highlighted by arrows). **e** Z-stack scan of a COA1@POR1 membrane where the cross sections in the xy, xz, and yz planes are laid out on the left and the 3D reconstruction is presented on the right (box size = 70 × 70 × 7 μm, color bar indicates height in z direction). **f** The contact angle (θ) of a COA1 droplet on PC surface underneath its dilute phase is 38 °. **g** The compositions of free COA1 droplets and in-pore COA1 are similar. Data are presented as mean ± SD ($n = 3$ independent experiments). **h** The FRAP curves for COA1@POR1, COA10@POR1, and COA17@POR1, and their corresponding free droplets. Sequential snapshots of a FRAP process of COA1@POR1 from −4 s (before bleaching) to 25 s of recovery, where the irradiation area is highlighted by a white circle. The coacervates in (**b**, **e**, **h**) are fluorescently labeled by 5 μM RhB. Scale bars = 20 μm (**b**) and 10 μm (**c**–**e**, **h**).

Table 1 | Summary of the coacervate systems (COA1 to COA19)

COA	Abbreviation	$\bar{\theta}$ (°)	SR	$\bar{K}_1$	$\bar{K}_2$
1	DTAB/PTS	43	5/5	9.5×10^2	3.2×10^2
2	BTPC/SDS	51	5/5	9.4×10^2	4.0×10^3
3	BTPC/PFOA	51	4/5	1.6×10^3	1.6×10^3
4	BZC/SA	nd	5/5	19	84
5	TBAB/SDS	nd	5/5	2.9×10^2	2.4×10^2
6	$GdCl_3$/PSS	9.8	5/5	36	29
7	ε-PL/PTS	27	5/5	2.1×10^2	2.5×10^3
8	PDDA/ATP	19	5/5	9.6	41
9	PAH/ATP	nd	5/5	42	15
10	PSBZB	8.9	5/5	0.48	0.30
11	PDDA/γ-PGA	20	3/5	2.4	1.0
12	ε-PL/PAA	51	4/5	5.9	2.5
13	PDDA/PAA	94	1/5	4.8	1.9
14	ε-PL/γ-PGA	nd	5/5	13	4.8
15	PAH/γ-PGA	nd	4/5	7.7	2.9
16	PAH/PAA	nd	4/5	7.3	2.7
17	PDDA/BSA	2.0	5/5	17	6.3
18	FUS-MBP	nd	5/5	6.5	2.1
19	Soy glycinin	nd	5/5	8.0	3.0

$\bar{\theta}$ indicates the averaged contact angle of a coacervate system on four kinds of membranes. SR represents the successful rate of CPC formation for a coacervate system with 5 kinds of pores, where 4/5, for example, means success on 4 kinds of pores. $\bar{K}1$ and $\bar{K}2$ are partitioning ratios averaged over small-molecule dyes and polymeric guests, respectively. nd is shorted for not determined.

DTAB stands for dodecyltrimethylammonium bromide, PTS for 1,3,6,8-pyrenetetrasulfonic acid tetrasodium salt, BTPC for benzyltriphenylphosphorus chloride, SDS for sodium dodecyl sulfate, PFOA for sodium perfluorooctanoate, BZC for benzethonium chloride, SA for sodium acrylate, TBAB for tetrabutylammonium bromide, PSS for poly(sodium-p-styrene sulfonate), ε-PL for ε-poly-L-lysine hydrochloride, PDDA for poly(dimethyldiallylammonium chloride), ATP for 5′-adenosine triphosphate disodium salt, PAH for poly(allylamine hydrochloride), PSBZB for a random copolymer of sulfobetaine methacrylate (SB) and sulfabetaine methacrylate (ZB), γ-PGA for poly-γ-glutamic acid, PAA for sodium polyacrylate, BSA for bovine serum albumin, and FUS-MBP for human fused in sarcoma (FUS) N-terminally tagged with maltose binding protein (MBP).

known condensates. COA1 to COA5 are made of small molecules, COA6 to COA8 of small molecules and synthetic polyelectrolytes, COA10 to COA16 of synthetic polyelectrolytes, and COA17 to COA19 of proteins (Fig. 3a–c). Our selections are made on the basis of their physicochemical disparity and commercial accessibility. Their water contents range from 20 to 70 wt% (Supplementary Fig. 5a and Supplementary Table 1). Their micropolarity is extracted by the fluorescence lifetime of a fluorophore (sulfonamide benzoxadiazole, SBD, Supplementary Fig. 6) and is represented as dielectric constant (ε) values[41], which varies from methanol-like to water-like ($\varepsilon \approx 30$–70) with an outlier being chloroform-like ($\varepsilon \approx 6$, Supplementary Fig. 5b and Supplementary Table 1). Their viscosity is measured by the fluorescence lifetime of a molecular rotor-based fluorophore (boron dipyrromethene, BODIPY, Supplementary Fig. 6)[41], ranging from ethylene glycol-like to honey-like (10 mPa s to 1 Pa s, Supplementary Fig. 5c and Supplementary Table 1). They are signified by low interfacial tensions (σ) on the order of 10 μN m^{-1} to 2 mN m^{-1} (Supplementary Fig. 5d and Supplementary Table 1). Our selection is therefore extensive enough to chart the accessible range of physical properties of known coacervates. As we will show next, the spontaneous formation of CPCs is rather insensitive to the physical properties of coacervates.

In addition to POR1, we further introduce 4 kinds of pores (Table 2 and Fig. 3d)[42]. POR2 are identical to POR1 except for its diameter ($\Phi = 50$ nm, close to the channel width of NPCs). POR3 are interconnected pores of a polydisperse size from 5 to 20 μm embedded in hydrophilic, polyvinyl alcohol (PVA) membranes. POR4 are foam-like voids of a polydisperse size from 20 to 60 μm dispersed in hydrophobic, polyurethane (PU) membranes. POR5 are the continuous space among the orthogonally interlaced, hydrophobic polyamide (PA) fibers. Pore morphology is confirmed by SEM pictures in Fig. 3e. We measure the contact angles θ of the coacervate droplets on non-porous PC, PVA, PA, and PU membranes submerged in their corresponding dilute phases, where $\theta < 90$ ° is observed for most combinations (Supplementary Table 2). The values averaged over four kinds of membranes ($\bar{\theta}$) are laid out in Table 1 and the distribution of individual θ is given in Supplementary Fig. 5e.

The combination of 19 coacervates with 5 pores can produce at most 76 kinds of possible CPCs, where successful self-deployment is observed in 66 combinations (successful rate = 87%, Supplementary Table 3). For example, COA1 can be efficiently deployed into POR2 to POR5 with pore occupancy approaching 100% regardless of the membrane chemistry, pore sizes, and void geometries (Fig. 3e). More examples can be found in Supplementary Fig. 7. The liquidity of COA10 and COA17 is not altered by the confinement of POR1 (Fig. 2h and Supplementary Fig. 3). Failed combinations frequently involve COA13 or POR2 (Supplementary Table 3). The former cases are caused by insufficient capillary drive P_c, where large θ are responsible especially in the cases of COA13 (4/5 failed, see also Supplementary Fig. 8). For the latter cases, the small size of POR2 likely contributes to kinetic hindrance in the formation of CPCs by highly viscous coacervates. We suspect that when the viscous coacervate droplets get in contact with a 50-nm pore, they cannot quickly displace the dilute phase inside the pore, rather they adhere to the membrane surface more readily. Other coacervate systems with low viscosity can easily fill the pores. Here we provide a few rules of thumb for the successful self-deployment in light of simple calculations in the continuum limit (Fig. 1e)[37]. The pores must be preferentially wetted ($\theta < 90$ °) by the coacervate rather than by the dilute phase, and the interfacial tensions should be large enough ($\sigma > 0.05$ mN m^{-1}) and pore size small enough ($\Phi < 100$ μm) to drive spontaneous imbibition and to keep the coacervates firmly adhered against gravity or moderate flow. As these criteria can be readily fulfilled, the self-deployment of coacervates into porous membranes is by large a universal phenomenon.

CPCs as a selective permeability barrier

Inspired by the selectivity of NPCs[6], we aim at CPCs that barricade most guest molecules but are permeable to a few targeted guests. In our case, the permeability (P) of a guest molecule through the coacervate phase is expected to be proportional to the product of partitioning ratio (K) between the coacervate and dilute phase and diffusivity (D) of the guest in the coacervate phase according to the solution-diffusion model[43], reading $P \propto K \times D$. K is an indicator of guest-coacervate affinity, in which the coacervate droplets provide an environment physicochemically distinct from the dilute phase to accumulate or exclude guests by equilibrium partitioning[25]. Table 1 lists K values averaged over small-molecule dyes ($\bar{K}1$) and polymeric guests ($\bar{K}2$) for the 19 coacervate systems (see Supplementary Table 4 for a complete data set). Please note that the K values are determined by UV-vis absorbance or fluorescence measurements (see the Methods section); in the latter case, the fluorescence intensity ratios are only approximate representation of K because the fluorescence intensity depends on the local environments the dye molecules reside in. Most systems can be categorized into inclusive coacervates that significantly enrich different kinds of guest molecules ($\bar{K}1$ and $\bar{K}2 \gg 1$). This broad-spectrum affinity likely originates from the possible coexistence of hydrophilic and hydrophobic microdomains and the presence of different kinds of intermolecular interactions (electrostatic, hydrophobic, and H-bonding). Such inclusiveness is counterproductive to the intended selectivity.

We thus look for a kind of exclusive coacervates that reject most guest molecules and notice a recently reported zwitterionic polymer (PSBZB, Fig. 3b) made of randomly arranged sulfobetaine

https://doi.org/10.1038/s41467-024-54510-9

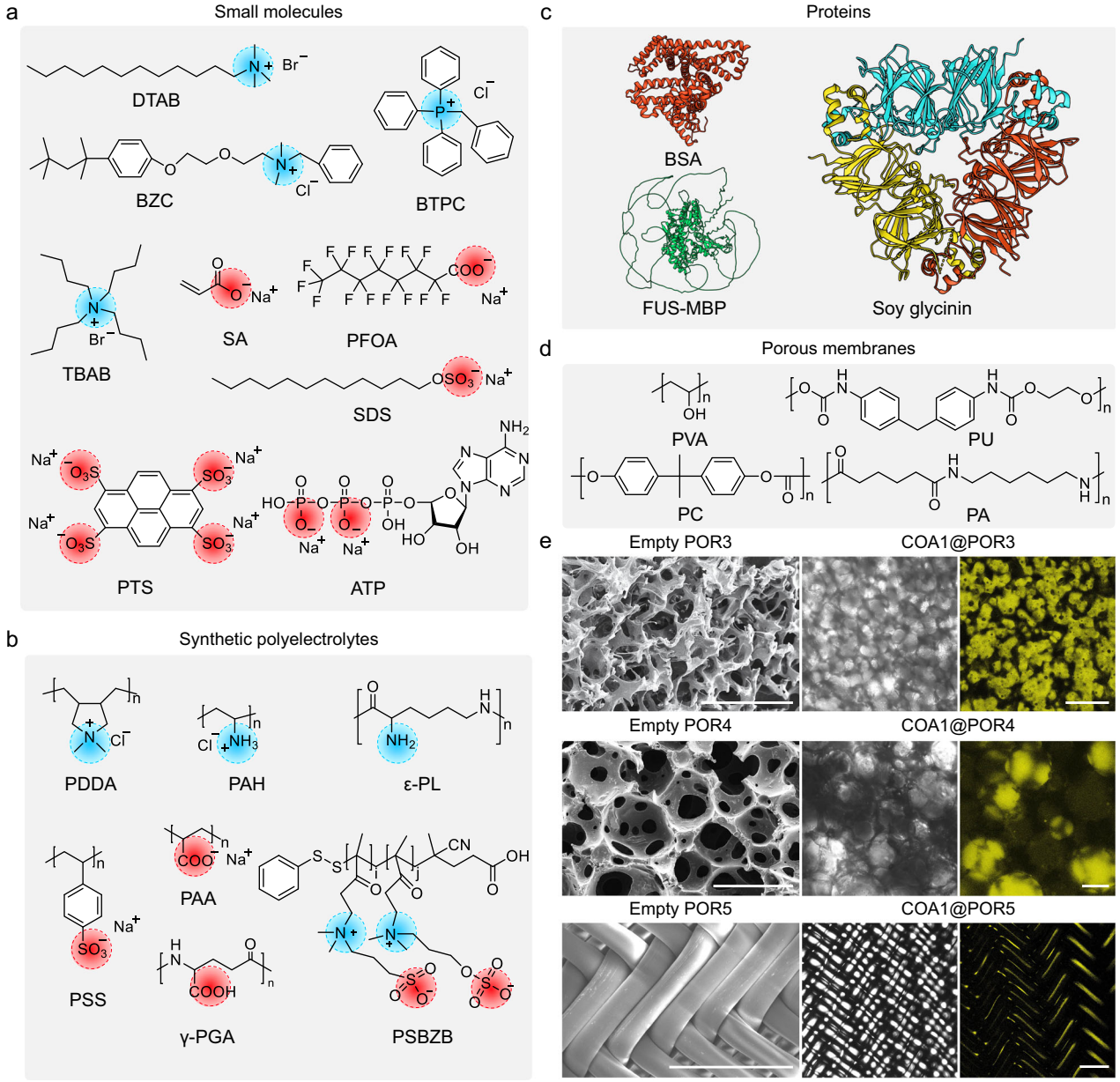

Fig. 3 | Molecular structures of the coacervate systems and porous membranes. Molecular structures of the coacervate constituents (**a**–**c**) and the membranes (**d**), where the positive and negative charges are highlighted by blue and red circles, respectively. The structure of FUS-MBP is generated by AlphaFold2, whose prediction on the intrinsically disordered region (IDR) may not be accurate. **e** SEM pictures of bare pores (POR3 to POR5) and optical images of the pores loaded with COA1 in the transmission and fluorescent channels, where COA1 is mixed with 5 μM RhB. Scale bars = 50 μm.

methacrylate (SB) and sulfabetaine methacrylate (ZB)[44]. We synthesize PSBZB (MW ~ 20 K, Supplementary Fig. 9) and confirm its self-coacervation via the electrostatic pairing between the zwitterionic monomers, where the coacervate droplets (denoted as COA10) are observed in Supplementary Fig. 9b. Zwitterionic polymers are well known for their superhydrophilicity and anti-fouling properties against proteins[45], hinting at their general repellence against various molecules. Indeed, COA10 droplets exclude most tested molecules with K values < 1 (Table 1 and Supplementary Table 4). Figure 4c shows that K values (as reflected by the ratio of fluorescence intensities inside and outside the coacervate droplets) of five guest molecules are all smaller than unity and that they increase in the order of PEG-20K, PEG-5K, BSA, RhB, and ε-PL (properties of these 5 guests are summarized in Supplementary Table 5). Presumably, the charges of SB and ZB are paired and saturated within the coacervates such that they cannot engage in additional interactions with guest molecules[44].

We then fabricate a permeability device compatible with a confocal microscope for in-situ, real-time observation of the permeation process (Fig. 4a)[10]. In this device, a COA10@POR2 membrane is placed

Table 2 | Comparison of 5 kinds of solid-state pores (POR1 to POR5) in terms of membrane chemistry, pore diameter (Φ) and pore morphology

POR	Membrane	Φ	Pore morphology
1	PC, hydrophobic	3 μm	dispersed, cylindrical
2	PC, hydrophobic	50 nm	dispersed, cylindrical
3	PVA, hydrophilic	5–20 μm	connected, sponge-like
4	PU, hydrophobic	20–60 μm	connected, foam-like
5	PA, hydrophobic	5–60 μm	space between fibers

PC stands for polycarbonate, PVA for polyvinyl alcohol, PU for polyurethane, and PA for polyamide.

https://doi.org/10.1038/s41467-024-54510-9

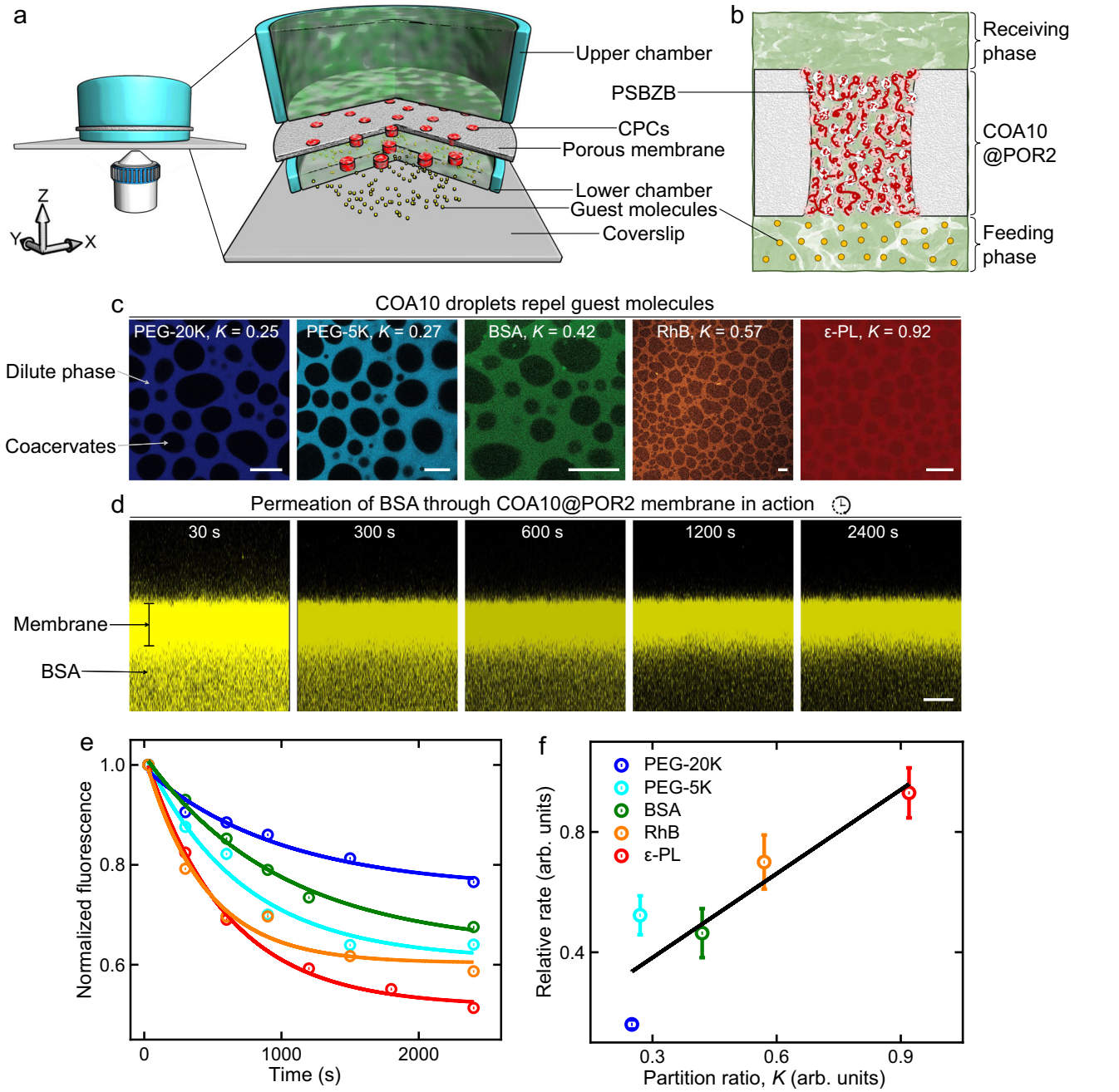

Fig. 4 | Selective permeation of CPCs. a A microscope-compatible, permeability device with a lower chamber, a CPC membrane, and an upper chamber. **b** A scheme showing the guest molecules in the feed phase tend to traverse the COA10@POR2 to reach the receiving phase. **c** False-color, fluorescence images to indicate the disfavored partitioning of PEG-20K (MW ~ 20 K, 0.04 g L^{-1}), PEG-5K (MW ~ 5 K, 0.04 g L^{-1}), BSA (MW ~ 65 K, 5 μM), RhB (MW = 479, 5 μM), and ε-PL (MW ~ 5 K, 0.01 g L^{-1}) into the COA10 droplets (4 g/L, 0.2 M NaCl, pH = 7.2). Two PEGs are tagged by HEMA-RhB, BSA by TRITC, and ε-PL by FITC. **d** Permeation of BSA across the COA10@POR2 membrane following a concentration gradient from the lower to the upper chambers. **e** The decay of normalized fluorescence intensity in the feeding phase for five different guests (dots) is fitted by an exponential function (lines) to give the rate constant (R). **f** Transport rate relative to that across bare pores (R/R_0) is plotted against the K values, where a liner fitting can reasonably match the data (black line). Data are presented as mean ± SD (n = 3 independent experiments). The blue, cyan, green, orange, and red in (**e**, **f**) correspond to PEG-20K, PEG-5K, BSA, RhB, and ε-PL as the guest molecules, respectively. Scale bars = 30 μm (**c**) and 5 μm (**d**).

in between a shallow, lower chamber that is immediately above a cover slip and a deep, upper chamber. Before experiment, the lower chamber is filled by an aqueous solution of fluorescent guest molecules and the upper chamber is loaded with the same solution in a small amount; the guest molecules are allowed to reach adsorption equilibrium on the membrane. Then the upper chamber is diluted ~83-fold to initiate guest transportation from the lower chamber (feed phase) to the upper chamber (receiving phase, Fig. 4b). The upper chamber can be considered as a sinking hole with a negligible dye concentration during the entire permeation period. Confocal scans in the xz plane are repeatedly performed to follow the permeation process, where the fluorescence of the membrane remains constant (Supplementary Fig. 10) and that of the feed phase continues to drop to the noise level as the guest molecules gradually traffic to the receiving phase (Fig. 4d

https://doi.org/10.1038/s41467-024-54510-9

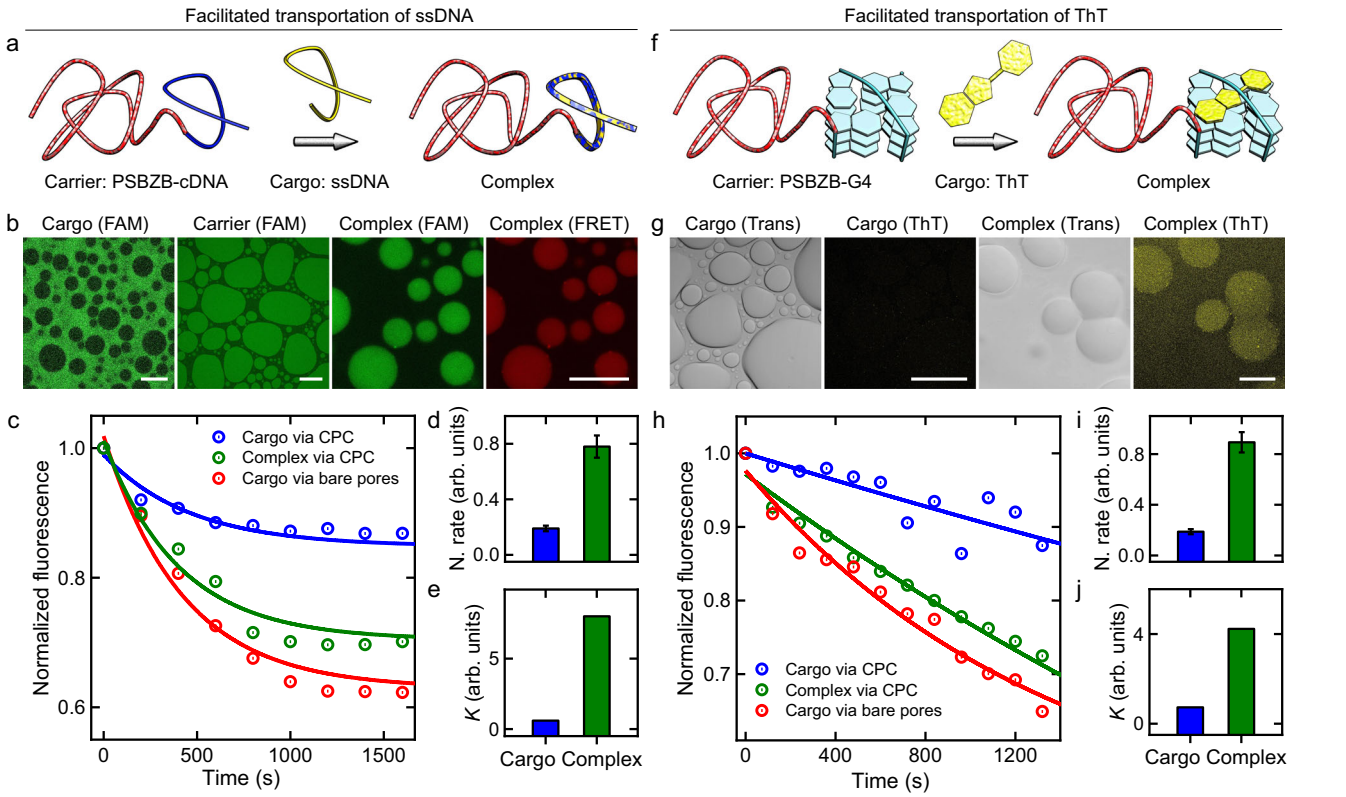

Fig. 5 | Facilitated transportation of two cargoes by two designer carriers. a A conjugated carrier, PSBZB (MW ~ 20 K)-complementary DNA (cDNA, MW ~ 6.4 K), binds the cargo, ssDNA (MW ~ 6.4 K), to form a complex. **b** Fluorescence images showing that the cargo (1 μM ssDNA) is rejected while the carrier and complex are enriched by the COA10 droplets (4 g/L, 0.2 M NaCl, pH = 7.2). FAM indicates the fluorescent tag, carboxyfluorescein. FRET (Förster resonance energy transfer) channel confirms the formation of complex and its enrichment to the droplets. **c** Decay of normalized fluorescence intensity for the transportation of the cargo across the bare pores (red dots), the cargo across COA10@POR2 (blue dots), and the complex across COA10@POR2 (green dots); exponential fittings are given by lines. Comparisons between the cargo and complex on the transport rate (normalized by the bare pore rate (**d**) and on the partitioning ratios (**e**). **f** A conjugated carrier, PSBZB-G4 (DNA G-quadraplex), binds the cargo, ThT, to form a complex. **g** Optical images of the transmission and fluorescence channels showing that the cargo (1 μM ThT, MW = 319) is rejected by the COA10 droplets (4 g/L, 0.2 M NaCl, pH = 7.2) and fluorescently dim and that the complex is enriched by the droplets and fluorescently bright. The fluorescence decay (**h**), normalized transport rates (**i**) and partitioning ratios (**j**) similar to panels (**c**–**e**), except that the cargo is now ThT. Scale bars = 50 μm (**b**, **g**). Data are presented as mean ± SD ($n = 3$ independent experiments, **d**, **i**).

for TRITC-BSA as the guest). This intensity drop is not caused by photobleaching as verified by a control experiment (Supplementary Fig. 11). The fluorescence intensity (I, proportional to the guest concentration) in the feeding phase for five different guests is recorded to quantify the permeation kinetics (Fig. 4e), which is fitted by an exponential decay to give the rate constant (R). Figure 4f plots relative rates (with respect to the bare pore values, R/R_0) of the guests against their K values, highlighting a strong dependence of R/R_0 on K. Rates across the bare pores are given in Supplementary Fig. 12. This roughly linear relationship is in line with the proportionality between permeability and partitioning ratio, $P \propto K$.

We then study the effect of monomer composition of PSBZB on guest partitioning and permeation by comparing three additional PSBZB polymers (PSBZB-2 to PSBZB-4 with SB: ZB = 1, 2, and 3, respectively) and with the original PSBZB with a SB: ZB = 0.5. Among them, PSBZB with the lowest SB ratio strongly rejects three guest molecules (RhB, BSA, and ssDNA) as compared to the other counterparts (Supplementary Fig. 13). This is in line with the notation that the similarity in charge densities and hydration between the cationic and anionic groups in ZB monomer imposes stronger ZB-ZB self-association to repel guest molecules, as compared to the SB monomer[44,46]. Permeation curves of the three guest molecules through bare pores or PSBZB-x@POR2 are given in Supplementary Fig. 14. Transport rates relative to the bare-pore values (R/R_0) are summarized in Supplementary Fig. 14d as a function of K, where a dependence of relative rates on K is obvious for PSBZB (the cyan line) but not for the other PSBZB molecules. We further conduct permeation experiments on two more coacervate systems (COA1 and COA17) to show that they can also act as liquid permeability barriers although the dependence of R/R_0 on K is not prominent (Supplementary Fig. 15).

Cargo transportation facilitated by designer carriers

While NPCs reject most macromolecular guests from cross-pore diffusion, they rely on nuclear pore receptors (NTRs) to bind specific macromolecular cargoes and to carry them across the NPC channel at a significant rate[1,10]. Motivated by such facilitated transportation, we intend to design synthetic carriers that can boost the passage rate of targeted cargoes across CPCs. Ideally, a carrier should recognize a cargo by forming a carrier-cargo complex efficiently and the complex shall partition favorably into the CPCs and traverse with ease. For the COA10@POR2 system that rejects most guest molecules, a PSBZB block can provide the required coacervate affinity via homopolymer interactions. Onto the PSBZB block we then conjugate two kinds of cargo-binding moieties to target a macromolecular and a small-molecule cargo, respectively (Supplementary Fig. 16 and 17).

The first cargo is a ssDNA of 19 bases (Fig. 5a) that are repelled by the COA10 droplets (the cargo panel in Fig. 5b, K = 0.4 in Fig. 5e). Its transportation across the CPCs, in comparison to bare pores, is significantly hindered by the presence of the in-pore coacervates (blue and red dots in Fig. 5c). We synthesize a diblock carrier consisting of a PSBZB moiety and a complementary DNA moiety (the PSBZB-cDNA chain in Fig. 5a), verify its successful conjugation (Supplementary

Fig. 18), and confirm its favorable partitioning in the droplets (the carrier panel in Fig. 5b). Formation of carrier-cargo complex via DNA hybridization is ascertained by Förster resonance energy transfer (FRET) imaging (the complex panels in Fig. 5b), where a donor and an acceptor are respectively tagged to the two complementary chains (Supplementary Fig. 19). As expected, the complex strongly enriches itself into the coacervate droplets (the complex panels in Fig. 5b, K = 8.1 in Fig. 5e) and traverses COA10@POR2 much faster than the ssDNA itself does (green dots in Fig. 5c). The fitted rate constants are normalized by the rate across the bare pore and are compared in Fig. 5d to highlight a ~5-fold boosting by the carrier.

The second cargo is a small molecular dye thioflavin T (ThT, Fig. 5f) disfavoring COA10 droplets (the cargo panels in Fig. 5g, K= 0.7 in Fig. 5j), whose permeation through COA10@POR2 is thus retarded (blue dots in Fig. 5h). Notably ThT by itself is fluorescently dim (Fig. 5g) and its K is determined by absorbance measurements. It was reported that ThT can strongly interact with DNA quadruplexes (G4s) in a 1/1 stoichiometry by predominantly stacking onto the top of G-tetrad and that the ThT-G4 complexes are fluorescently bright[47]. We thus conjugate DNA G4s to the PSBZB moiety to produce a carrier that can effectively take on ThT molecules (Fig. 5f). The resultant complex emits strong fluorescence and is moderately enriched in the COA10 droplets (the complex panels in Fig. 5g, K = 4.2 in Fig. 5j), and it can transit COA10@POR2 at a rate much faster than ThT itself does (green dots in Fig. 5h corresponding to a 2-fold promotion in Fig. 5i). For both the ssDNA and ThT, their corresponding complexes are significantly larger yet permeate the CPC faster. This is in line with the previous note that portioning ratio plays a dominant role over guest size to determine the permeability.

We then test if this specific cargo transportation can proceed in the presence of an interfering cargo by setting the ssDNA as the targeted cargo and a cationic polyelectrolyte, ε-PL, as the interfering cargo. As shown in Supplementary Fig. 20, COA10@POR2 with a carrier (PSBZB-cDNA) can facilitate the translocation of ssDNA while restricting the permeation of ε-PL. Two negative controls, COA1@POR2 and COA17@POR2 without proper carriers, cannot efficiently distinguish ssDNA and ε-PL. Moreover, we expect that it is possible to release the cargoes, ssDNA or ThT, by heating the receiving phase above the respective melting temperatures T_m of dsDNA or G4 (Supplementary Fig. 17 and Supplementary Table 6). This expectation is based on the following reasoning. The formation of double-stranded DNA and G4 relies on complementary base pairing, where the main driving force (H-bonding) is sensitive to temperature. Heating weakens the H-bonding such that dsDNA dissociates into single strands above T_m[48], releasing the cargo. Heating can also impair the formation of antiparallel structures for G4[49], consequently releasing ThT.

Dynamic reconfigurations of CPCs

It is their intrinsic nature that liquid coacervates may transition into dissolved or solid-like states in response to environmental cues such as temperature, pH, and redox stimuli[50]. For example, synthetic coacervates or biomolecular condensates can be dissolved with a lower or upper critical solution temperature (LCST or UCST) such that the condensed phase reverts to a dissolved state; this kind of transition is usually reversible[51]. They can also shift into gellike, glassy, or crystalline states where the solutes are dynamically arrested or covalently fixated; this liquid-to-solid transition (often irreversible) may lead to the formation of aberrant protein aggregates or amyloid fibrils in vivo, causing neurodegenerative diseases[24]. We postulate that, in the case of CPCs, the dissolved, liquid, and solid states shall respectively impose little, intermediate, and severe barriers for guest transportation (Fig. 6a).

To demonstrate this idea, we focus on COA17 (Table 1) in which a polycation, polydiallyldimethylammonium chloride (PDDA, Fig. 3b), and a negatively charged protein, bovine serum albumin (BSA, Fig. 3c), undergo complex coacervation as driven by electrostatic attractions and entropic gain due to counterion release[52]. pH plays a pivotal role in the coacervation behavior as it determines the surface charge of BSA (pI = 4.9). At a low pH, BSA (positively charged) cannot interact with PDDA strongly, giving a homogenous solution with no sign of coacervate droplets (dissolved state for pH = 2 in Fig. 6b). At an intermediate pH, BSA is moderately negatively charged to interact with PDDA to an appropriate extent, producing a turbid suspension of liquid coacervates (liquid state for pH = 5, 7, and 10 in Fig. 6b). At a high pH, BSA is overly charged to complex with PDDA in an irreversible manner, yielding gellike particles or solid precipitates (solid state for pH = 13 in Fig. 6b). Next, we construct COA17@POR1 at pH = 7 as confirmed by the colocalization of pores and coacervates observed by the transmission and fluorescence channels, respectively (Fig. 6c). Adjusting the solution pH to 2 dissolves the coacervates and dissipate their fluorescence, reaching a dissolved state (Fig. 6c). Shifting the solution pH to 13 precipitates the coacervates in the pores, attaining a solid-like state (Fig. 6c and the SEM picture in dry state in the inset). The dissolved, liquid, and solid states are further confirmed by FRAP experiments to assess the diffusivity of RhB (Supplementary Fig. 21). Correspondingly, transportation rates of two guests (RhB and PEG-5K) across the CPCs at different states are measured to be high, moderate, and low for the dissolved, liquid, and solid-like states, respectively (Fig. 6d).

Healing of liquid materials refers to the ability of certain liquids to repair damage or to recover their original properties preferably without external intervention[53]. In our case, a COA10@POR1 membrane is placed in the permeability device (Fig. 4a) where a tiny amount of extra coacervate droplets is presented in the lower chamber (upper panels in Fig. 6e). We punctuate the membrane by an array of microneedles to create through holes (10-40 μm in diameter) that are not filled by the coacervates (middle panels in Fig. 6e). Sonication or gentle shaking is applied to the device to redisperse the sedimented, extra droplets such that they can approach and fill the void (lower panels in Fig. 6e). Almost all the holes in a membrane can be refilled (Supplementary Fig. 22). The healed membrane restores its original permeability. Such healing behavior is also observed for COA1@POR1 and COA17@POR1 systems (Supplementary Fig. 23).

Discussion

We are inspired by NPCs to construct coacervate-pore complexes (CPCs) that can control the cross-pore transportation by guest-coacervate affinity. It is the liquid coacervates of CPCs that is drastically different from the solid fillers (surface-grafted brushes or crosslinked polymers) of native NPCs or their synthetic mimicries (Fig. 1). There are four major features that originate from such liquid nature. First, self-deployment of CPCs is a spontaneous, capillarity process in which the dilute phase in the pores is fully displaced by the coacervates (Fig. 1e). This process is effortless as thermodynamically driven by preferential wetting of pore surfaces by the coacervates over the dilute phase, whereas the fabrication of solid constructs relies on potentially complicated assembly or synthesis steps to fixate the pore fillers. The liquid coacervates can fill the pores regardless of their sizes or geometries, yet the surface-grafted brushes can only work on small pores (<100 nm)[9–12] and the crosslinked gels cannot easily fit into porous geometries of complexity.

Second, self-deployment of CPCs is universal as strongly suggested by the dominating cases of favorable wetting conditions of different coacervate/membrane combinations (Fig. 3) and by the high successful rate of CPC formation (87%, Supplementary Table 3). This universality is particularly meaningful because the coacervate systems can provide almost infinite possibilities of constituent chemistry to target specific guests and the choices of pores are virtually unlimited from a large pool of commercially available, processable porous materials[42]. While the native NPCs and their mimicries are limited to FG-rich proteins and a few kinds of synthetic polymers[9–15], the current

https://doi.org/10.1038/s41467-024-54510-9

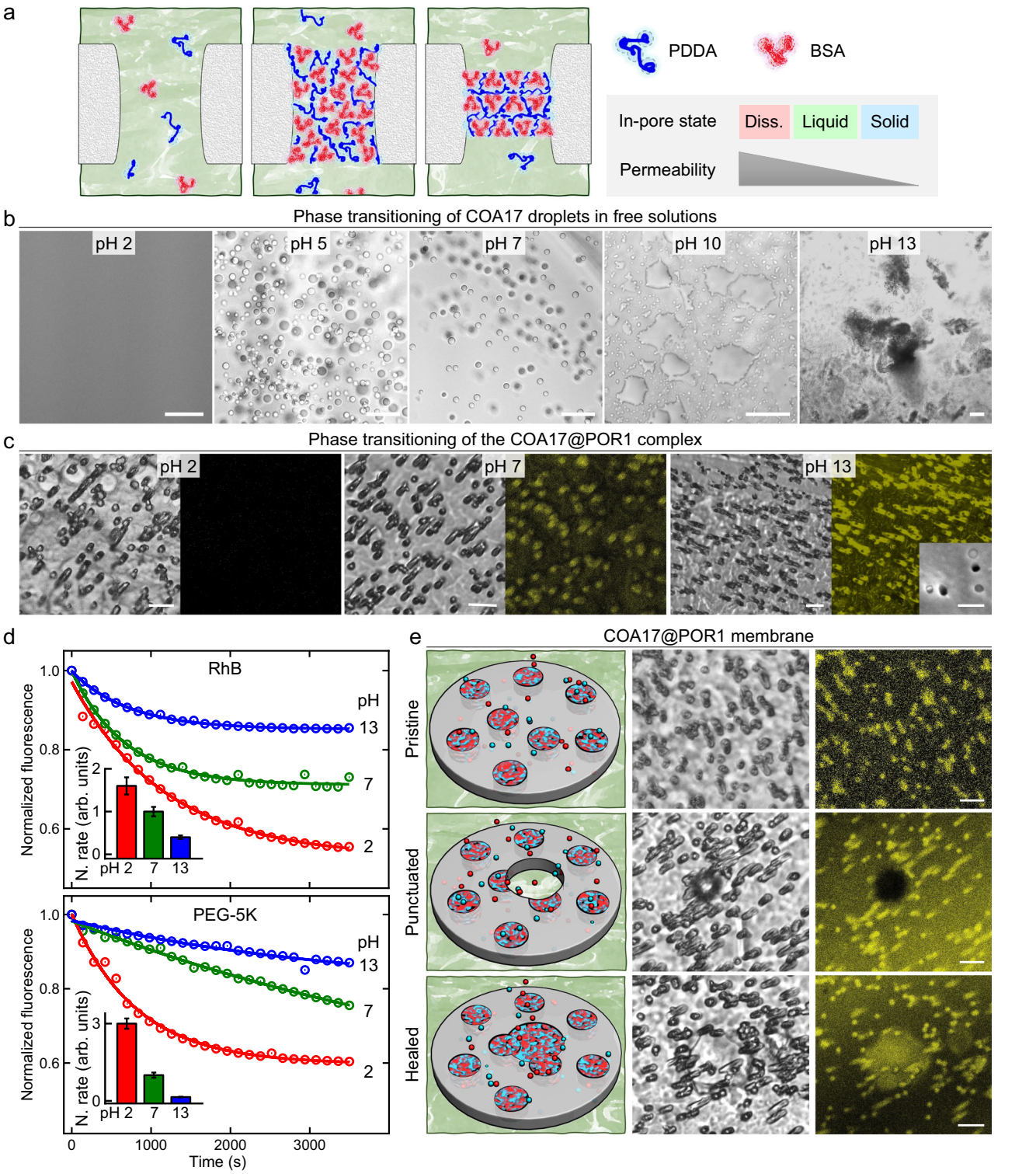

Fig. 6 | Dynamic reconfiguration of CPCs. a Schematic illustration of the phase transitioning of COA17 to a dissolved or a solid state, regulating the CPC permeability. **b** Optical observation of phase transitions of free COA17 droplets into a dissolved state at pH = 2 and into a solid state at pH = 13. **c** Correspondingly, the in-pore coacervates reach a dissolved, liquid, and solid states at acidic, neutral, and basic conditions as confirmed by optical images in the transmission and fluorescence channels and by a SEM picture. **d** Fluorescence decay curves for 5 μM RhB and 0.1 g L^{-1} PEG-5K to pass the COA17@POR1 membranes at pH = 13 (blue), 7 (green), and 2 (red), respectively. The lines are exponential fittings. The insets compare the transportation rates normalized by the rate at pH = 7. Data are presented as mean ± SD ($n = 3$ independent experiments). **e** Schematic drawings and optical images of the transmission and fluorescence channels for a COA17@POR1 membrane at its pristine, punctuated, and healed states, respectively. Scale bars = 50 μm (**b**) and 10 μm (**c**, **e**). The coacervates in (**c**, **e**) are fluorescently labeled by a trace amount of TRITC-BSA.

CPCs hold substantial chemical richness to encompass the large family of intrinsically disordered proteins (IDP), nucleic acids, polysaccharides, synthetic polyelectrolytes, small molecules, and even nanoparticles given their tendency to undergo liquid-liquid phase separation to produce coacervates[39,40].

Third, CPCs can block the cross-pore traffic of most guest molecules while permitting that of a few targeted guests, as intended for a synthetic mimicry of NPCs. Such selective permeability is demonstrated for an exclusive coacervate system (COA10, Fig. 4) with both similarities and differences to the native NPCs. In the case of NPCs, the FG-rich proteins might assemble into a hydrogel-like, crosslinked network that acts as a passive mesh to control guest permeation by guest-NPC affinity and guest size[13,14,27,54]. Gorlich et al. in a seminal work systematically engineered the surface chemistry of variants of GFP to tune their guest-NPC protein affinities, and they conclusively established the dependence of permeability on the affinity[27]. The NPCs also reject guests larger than the mesh size but allow the passage of smaller guests[1]. In our case, the dependence of permeability on guest-coacervate affinity is amply demonstrated ($R \propto K$ in Fig. 4f), while the effect of guest size is not obvious. No clear trend on size is observed for the 5 guests with hydrodynamic radii (r_h) ranging from 0.7 nm (RhB) to 3.9 nm (BSA, Fig. 4f). This is probably due to the liquid nature of coacervates; the polymer chains dynamically reorganize such that the effective meshes significantly fluctuate, thus imposing a loose constraint on guest molecules as compared to the tight restriction by the crosslinked meshes of FG-proteins. And it is, to a less extend, due to the small, effective mesh size of COA10 which is estimated to be smaller than 1 nm given the high polymer concentration in the coacervates (~50 wt%, Supplementary Table 1); this mesh size can barely distinguish guests with $r_h > 1$ nm. In addition, we synthesize conjugated carriers to facilitate the transportation of targeted cargoes (Fig. 5), playing a role akin to that of NTRs. Notably the carrier-cargo complexes are significantly larger yet permeate faster, echoing the dominate role of affinity over guest size. In addition, we have also summarized three design principles to construct CPCs (Supplementary Fig. 24). Stage 1: $\theta < 90°$ for CPC formation by capillary infiltration. Stage 2: Select CPC systems with a strong dependence of permeability rate (P) on the guest-coacervate affinity (K) that allow selective, cross-pore transportation. Stage 3: Synthesize carriers with a coacervate-affine and a cargo-affine moiety to facilitate the transportation of specific cargoes.

Finally, the liquid nature endows CPCs with reconfigurable capabilities of phase transitioning and dynamic healing (Fig. 6). Relevantly, surface-grafted brushes were reported in a few cases to respond to temperature or pH to regulate permeation via configurational changes between the collapsed and extended molecular states[9,16,17]. For CPCs, the phase transitioning of in-pore coacervates from a liquid to a dissolved or a solid state is expected to drastically upregulate or downregulate the permeability, respectively. Should any damage occur on a CPC membrane to create leaky holes, we can redisperse the coacervate droplets to fill the newly perforated openings and restore the permeability; such healing can be hardly attained by any solid constructs. There is a concern that some features of CPCs can be reproduced by low-crosslinking gels or polymer solutions, we would argue that 1) a polymer solution can hardly act as a permeation phase and 2) there are at least two features, spontaneous formation and healing at newly created voids, cannot be readily attained by the low-crosslinking gels. As an NPC mimicry, the in-pore phase must be drastically distinctive from the feeding and the receiving phase; yet a polymer solution in pores cannot hold itself as it will be dissolved by the dilute phases. The polymer solution has to be phase-separated from the dilute phase, which is actually the case of LLPS of coacervation as we have studied. For a low-crosslinking gel, it is not expected to spontaneously form inside the pores; a particular synthesis procedure is required to implement the gel inside the pores. This is different from the current CPCs. Also, a low-crosslink gel is not expected to reconfigure itself to fill the newly created voids.

In summary, the current marriage between the liquid coacervates and solid-state pores is quite productive in the sense that it can secure the fundamental functions of NPCs (selective permeation and facilitated transportation) and can complement the solid constructs with spontaneous formation, dynamic healing, and phase transitioning. Critical to such complementation is the liquid nature of coacervates, which ensures the fluidity and dynamical reconfigurability of the pore fillers. Looking forward, we expect the current work to provide a practical guide for constructing liquid constructs of NPC mimicries by employing a large pool of synthetic coacervates and biomolecular condensates[39,40]. The observed universality also hints at the possible functionality of permeation of intracellular condensates[26].

Methods

Materials

Porous membranes. POR1 and POR2 are polycarbonate (PC) membranes purchased from Sterlitech (pore size = 3 μm and 50 nm, thickness = 9 and 6 μm, respectively; and more specifications can be found in https://www.sterlitech.com/hydrophilic-polycarbonate-membrane-filter-pct00113100.html). Polyvinyl alcohol (PVA) membranes, polyurethane (PU) membranes, and polyamide (PA) membranes were purchased from suppliers on Taobao, China.

Guest molecules. Rhodamine B (RhB, 97%), Rhodamine 6 G (Rh6G, AR), methyl orange (MO, 98%), safranine T (ST, AR), methylene blue (MB, 98%), thioflavin T (ThT, 97%) were purchased from Macklin, China. Brilliant Blue R (BBR, AR) was purchased from Shanghai D&B Biological Science and Technology Co., China. Sulfonamide benzoxadiazole (SBD) and boron dipyrromethene (BODIPY) were synthesized for the determination of micro polarity and micro viscosity of condensed phases, respectively, according to previous reports[41].

Reagents for synthesis. Sulfobetaine methacrylate (ZB) and HEMA-RhB were synthesized according to a previously published protocol[44]. [2-(methacryloyloxy)ethyl]dimethyl-(3-sulfopropyl) (SB) was purchased from Aladdin, China. 4,4′-azobis(4-cyanovaleric acid) (ACVA, ≥98%) and 4-cyano-4-(phenylcarbonothioylthio)pentanoic acid (CPA, ≥97%) were obtained from Bidepharm, China. Ethylene glycol methyl ether methacrylate (95%), 1,3-propanediol cyclic sulfate (TMS, 98%), N-(3-dimethylaminopropyl)-N′-ethylcarbodiimide hydrochloride (EDC, ≥98%), sodium acetate (≥99%), and N-hydroxysuccinimid (NHS, ≥99%) were purchased from Sigma Aldrich, USA. Different DNA sequences were purchased from GENEWIZ, China (see Supplementary Table 6 for sequences).

Coacervate constituents. 1,3,6,8-pyrenetetrasulfonic acid tetrasodium salt (PTS, 97%), benzethonium Chloride (BZC, ≥97%), 5′-adenosine triphosphate disodium salt (ATP, 98%), and poly (dimethyldiallylammonium chloride) (PDDA, Mw ~100,000–200,000, 20 wt.% aqueous solution) were purchased from Aladdin, China. Dodecyltrimethylammonium bromide (DTAB, 99%), benzyltriphenylphosphorus chloride (BTPC, 99%), $GdCl_3{\cdot}6H_2O$ (99%), sodium perfluorooctanoate (PFOA, 97%), sodium acrylate (SA,97%), tetrabutylammonium bromide (TBAB, 99%), ε-Poly-L-lysine hydrochloride (ε-PL, Mw <5000, 95%), poly(allylamine hydrochloride) (PAH, Mw ~ 15,000, 98%), bovine serum albumin (BSA, 96%), sodium polyacrylate (PAA, Mw 3000 ~ 5000), poly(sodium-p-styrene sulfonate) (PSS, Mw ~80,000), Tris-HCl (1 M, pH = 7.4) buffer and PBS buffer were purchased from Macklin, China. γ-Poly (L-glutamic acid) (γ-PGA, Mw ~ 10000, 98%) was purchased from Shanghai D&B Biological Science and Technology Co., China. MBP-FUS were expressed in BL21(DE3) cells and purified using a HisTrap FF crude column (GE Healthcare) following a published protocol[55]. Soy glycinin was obtained from defatted soybean flakes (Yuwang Group, China) by precipitation at pH 4.5 using the procedure detailed elsewhere[56,57].

Instruments

Nuclear Magnetic Resonance (NMR). The synthesized powders of PSBZB and ZB were dried under vacuum, dissolved in 1 M NaCl D_2O solution, and analyzed on a 500 MHz NMR spectrometer (Bruker, Germany). Scanning electron microscopy (SEM) observation by JSF-7900 (JEOL, Japan). The porous membranes or CPC membranes were dehydrated and coated with a layer of platinum before observation Contact angle measurements by JC2000D (POWEREACH, China). The clean POR sample was placed on the surface of the glass and fixed, then placed in a transparent pool with a dilute phase, and a droplet of 3 μL coacervate phase was dropped gently on the POR sample surface. A photo was taken when the droplet shape reached equilibrium and subjected to analysis by a type. Optical images were taken by one of two confocal laser scanning microscopy (CLSM) systems, Leica TCS SP8 STED or Zeiss SLM 880. Fluorescence lifetime imaging microscopy (FLIM) images were recorded by Leica TCS SP8 STED. Fluorescence recovery after photobleaching (FRAP) was measured by Zeiss SLM 880. All the experiments were conducted at room temperature.

Preparation of COA microdroplets and CPCs

The complex coacervate systems (COA1 to COA9 and COA11 to COA17) were prepared by sequentially adding solutions of the positively charged constituents, salts, and the negatively charged constituents to a centrifuge tube to reach desired concentrations listed in Supplementary Table 1, followed by 1 min vertexing. The simple coacervate systems (COA10 and COA18) were prepared by diluting high-concentration, homogeneous solutions with DI water. COA19 suspensions were prepared by mixing 100 mg mL^{-1} soy glycinin aqueous solution with 0.4 M NaCl solution. For CPCs, we immersed a porous membrane into a coacervate suspension and then sonicated the sample for 1 min such that the coacervate droplets could fill the pores. For fluorescence observations, COA1 to COA11, COA13 to COA15, and COA19 were labeled by adding RhB, COA12 by adding FITC-ε-PL, and COA16 by adding TRITC-PAH at ~5 μM. Beforehand, the membranes were cleaned by a surfactant solution, ethanol, and then DI water. We observe no trapped air or noticeable contaminants for the smallest pore (POR2) when the membranes are immersed in the dilute phase of coacervate systems. All the experiments are conducted at 25 °C.

Determination of coacervate compositions

For free coacervates, a suspension of coacervate droplets and the dilute phase are left still in a separatory funnel until the coacervate phase is fully layered (typically in 24 h). We then extract the coacervate layer and take a portion of it to measure the water content by weight loss during drying in a vacuum oven at 100 °C for 48 h. We dissolve another portion of the coacervate layer in a 1 M NaCl solution in D_2O to determine concentrations of the constituent molecules predominantly by NMR. Whenever possible, we prefer to determine the constituent concentration by UV-vis absorbance such as in the case of PTS of COA1. For in-pore coacervate, the coacervate-loaded membranes are rinsed by dilute phase three times to remove extra coacervates on membrane surfaces, and the residual dilute phase is removed by gentle wiping with tissue papers. Water content is determined by weight loss during drying in a vacuum oven at 100 °C for 48 h. We then submerge the membranes into a 1 M NaCl solution in D_2O for 10 min with sonication such that the in-pore coacervates are dissolved and constituent molecules are released from the pores. The constituent concentrations are determined by NMR or UV-vis absorbance.

Microviscosity and micropolarity

We added 2.5 mg/L BODIPY dye (which is viscosity sensitive) to glycerol/water mixtures with various viscosities and measured the fluorescence lifetime at 488 nm excitation by Leica TCS SP8 STED. The lifetime is plotted as a function of viscosity to obtain a standard curve, which is fitted by a linear equation. We then record the lifetime of BODIPY in the coacervate phase and calculate the microviscosity by the fitting equation. Before measurements, the dye is allowed to reach equilibrium partitioning into the coacervate phase for 1 h. We obtain micropolarity with similar procedures, where the dye is SBD and the standard curve is fitted by a logarithmic equation.

Determination of partitioning ratios (K) of guest molecules in the coacervate and dilute phases

We used a bulk assay when the coacervate samples can be prepared in a sufficient quantity (>10 mL) or a droplet assay otherwise to measure the partitioning ratios (K). In the bulk assay, a coacervate suspension is kept still in a burette to reach complete phase separation, from which the volume ratio ($V_{c/d}$) between the coacervate and dilute phases is determined. Then, guest molecules are added to the coacervate suspension in a centrifuge tube at a concentration of C_0 (generally ~5 μM). Phase separation and equilibrium partitioning are finished by centrifuge at $7155 \times g$ for 10 min and static incubation for 24 h. 10 μL supernatant (the dilute phase) is collected and diluted in a cuvette for UV-vis measurements. The guest concentration in the dilute phase (C_d) is determined by absorbance via predetermined standard curves. Finally, K is calculated by $K = \frac{(C_0 - C_d) + V_{c/d} C_0}{V_{c/d} C_d}$. In the droplet assay, we add fluorescent guests to the coacervate suspension and observe the fluorescence intensity inside and outside the droplets with a confocal microscope. The intensity ratio is an approximation of the actual portioning coefficient. However, we note that the fluorescence intensity ratio does not necessarily reflect the partitioning of dye molecules accurately because their emission may depend on local environment. In both assays, measurements are repeated on 3 identically prepared samples and the average values are reported.

Synthesis of PSBZB and PSBZB-RhB

The copolymers were synthesized via RAFT copolymerization using ACVA as initiator and CPA as RAFT agent. 6.72 g of SB, 13.2 g of ZB, 48 mg of CPA, and 14 mg of ACVA were dissolved in 80 g of 20/80 vol/vol ethanol/acetic buffer (pH = 4.5 with 3 M NaCl) and poured into a flask. The mixture was purged with nitrogen for 20 min and then heated to 65 °C for 24 h under constant stirring. The reaction mixture was dialyzed against 1 M NaCl for 3 days with a dialysis tubing (JIELEPU, molecular weight cut-off (MWCO) = 3.5 K Da) by frequently changing the aqueous solution. The final polymer solutions were filtered with a 0.45 μm pore-size nylon membrane and stored at −20 °C[44]. PSBZB-RhB was synthesized by adding previously synthesized HEMA-RhB (10 μg mL^{-1}) into the initial reaction mixture. The molecular weight of PSBZB measured by static light scattering is ~ 20,000 g mol^{-1}.

Polymer – DNA conjugation

The carboxylic end group of PSBZB was linked to the amine end group of oligonucleotides via the EDC/NHS mediated conjugation. Typically, a PSBZB solution (60 g/L, 1 M NaCl, 340 μL) was mixed with an NHS/EDC solution (4.9 mg NHS and 4.8 mg EDC in 340 μL 0.2 M MES buffer with 1 M NaCl, pH = 6.0), followed by incubation at room temperature. The mixture was then adjusted to pH = 7.2 and mixed with a 200 μL oligonucleotides solution (100 nmol cDNA or G4s in a 5× PBS buffer), which was allowed for reaction for 1 h. Finally, 40 μL ethanolamine was added to the solution and shaken at room temperature for 30 min[44,47].

Permeability through CPCs

The device used for guest molecules to pass through CPCs is shown in Fig. 4a. Bonded to the glass coverslip is a square piece of ~25 μm thick optically clear double-sided tape with a 6 mm diameter hole, forming the lower chamber of a volume ~3 μL. A CPC membrane was placed on top of the tape and a plastic container with a 6 mm diameter hole and 10 mm thickness was positioned on the top of the membrane, forming

the upper chamber. The device was placed on a confocal microscope and observed with a ×20 objective lens.

Membrane punctuation

After a membrane is loaded with coacervates, we punctuate it with an electric microneedling device that was commonly used for skincare. An array of microneedles is driven by an electric motor to vibrate vertically on a membrane, repeatedly penetrating the membrane. As such, the created holes vary in size (from 10 to 40 μm).

Reporting summary

Further information on research design is available in the Nature Portfolio Reporting Summary linked to this article.

Data availability

The authors declare that the data supporting the findings of this study are available within the paper and its Supplementary Information files. The data is also available from the corresponding authors on request. Source data are provided with this paper.

References

1. Hoogenboom, B. W. et al. Physics of the nuclear pore complex: Theory, modeling and experiment. *Phys. Rep.* **921**, 1–53 (2021).
2. Kabachinski, G. & Schwartz, T. U. The nuclear pore complex – structure and function at a glance. *J. Cell Sci.* **128**, 423–429 (2015).
3. Schwartz, T. U. Solving the nuclear pore puzzle. *Science* **376**, 1158–1159 (2022).
4. Kim, S. J. et al. Integrative structure and functional anatomy of a nuclear pore complex. *Nature* **555**, 475–482 (2018).
5. Ng, S. C., Güttler, T. & Görlich, D. Recapitulation of selective nuclear import and export with a perfectly repeated 12mer GLFG peptide. *Nat. Commun.* **12**, 4047 (2021).
6. Hulsmann, B. B., Labokha, A. A. & Görlich, D. The permeability of reconstituted nuclear pores provides direct evidence for the selective phase model. *Cell* **150**, 738–751 (2012).
7. Andersson, J. et al. Pore performance: artificial nanoscale constructs that mimic the biomolecular transport of the nuclear pore complex. *Nanoscale Adv.* **4**, 4925–4937 (2022).
8. Rush, C., Jiang, Z., Tingey, M., Feng, F. & Yang, W. Unveiling the complexity: assessing models describing the structure and function of the nuclear pore complex. *Front. Cell Dev. Biol.* **11**, 1245939 (2023).
9. Caspi, Y., Zbaida, D., Cohen, H. & Elbaum, M. Synthetic mimic of selective transport through the nuclear pore complex. *Nano Lett.* **8**, 3728–3734 (2008).
10. Jovanovic-Talisman, T. et al. Artificial nanopores that mimic the transport selectivity of the nuclear pore complex. *Nature* **457**, 1023–1027 (2009).
11. Kowalczyk, S. W. et al. Single-molecule transport across an individual biomimetic nuclear pore complex. *Nat. Nanotechnol.* **6**, 433–438 (2011).
12. Ketterer, P. et al. DNA origami scaffold for studying intrinsically disordered proteins of the nuclear pore complex. *Nat. Commun.* **9**, 902 (2018).
13. Frey, S., Richter, R. P. & Görlich, D. FG-rich repeats of nuclear pore proteins form a three-dimensional meshwork with hydrogel-like properties. *Science* **314**, 815–817 (2006).
14. Frey, S. & Görlich, D. A saturated FG-repeat hydrogel can reproduce the permeability properties of nuclear pore complexes. *Cell* **130**, 512–523 (2007).
15. Kim, M. et al. Artificially engineered protein hydrogels adapted from the nucleoporin Nsp1 for selective biomolecular transport. *Adv. Mater.* **27**, 4207–4212 (2015).
16. Huang, K. & Szleifer, I. Design of multifunctional nanogate in response to multiple external stimuli using amphiphilic diblock copolymer. *J. Am. Chem. Soc.* **139**, 6422–6430 (2017).
17. Svirelis, J. et al. Stable trapping of multiple proteins at physiological conditions using nanoscale chambers with macromolecular gates. *Nat. Commun.* **14**, 5131 (2023).
18. Keating, C. D., Martin, N. & Santore, M. M. Editorial overview: Coacervates and membraneless organelles. *Curr. Opin. Colloid Interface Sci.* **56**, 101527 (2021).
19. Banani, S. et al. Biomolecular condensates: organizers of cellular biochemistry. *Nat. Rev. Mol. Cell Biol.* **18**, 285–298 (2017).
20. Xu, C. et al. Living material assembly of bacteriogenic protocells. *Nature* **609**, 1029–1037 (2022).
21. Yang, S. Y. et al. Steering coacervation by a pair of broad-spectrum regulators. *Acs Nano* **13**, 2420–2426 (2019).
22. Chen, X. X. et al. Optothermally Programmable liquids with spatiotemporal precision and functional complexity. *Adv. Mater.* **34**, 2205563 (2022).
23. Su, Q., Mehta, S. & Zhang, J. Liquid-liquid phase separation: Orchestrating cell signaling through time and space. *Mol. Cell* **81**, 4137–4146 (2021).
24. Shin, Y. & Brangwynne, C. P. Liquid phase condensation in cell physiology and disease. *Science* **357**, 1253–1263 (2017).
25. Mountain, G. A. & Keating, C. D. Formation of multiphase complex coacervates and partitioning of biomolecules within them. *Biomacromolecules* **21**, 630–640 (2020).
26. Wei, M. T. et al. Phase behaviour of disordered proteins underlying low density and high permeability of liquid organelles. *Nat. Chem.* **9**, 1118–1125 (2017).
27. Frey, S. et al. Surface properties determining passage rates of proteins through nuclear pores. *Cell* **174**, 202–217 (2018).
28. Schmidt, H. B. & Görlich, D. Transport selectivity of nuclear pores, phase separation, and membraneless organelles. *Trends Biochem. Sci.* **41**, 46–61 (2016).
29. Celetti, G. et al. The liquid state of FG-nucleoporins mimics permeability barrier properties of nuclear pore complexes. *J. Cell Biol.* **219**, e201907157 (2020).
30. Dekker, M., Van der Giessen, E. & Onck, P. R. Phase separation of intrinsically disordered FG-Nups is driven by highly dynamic FG motifs. *Proc. Natl Acad. Sci. USA* **120**, e2221804120 (2023).
31. Yu, M. et al. Visualizing the disordered nuclear transport machinery in situ. *Nature* **617**, 162–169 (2023).
32. Branco, L. C., Crespo, J. G. & Afonso, C. A. M. Highly selective transport of organic compounds by using supported liquid membranes based on ionic liquids. *Angew. Chem. Int. Ed.* **41**, 2771–2773 (2002).
33. Kocherginsky, N. M., Yang, Q. & Seelam, L. Recent advances in supported liquid membrane technology. *Sep. Purif. Technol.* **53**, 171–177 (2007).
34. Taylor, N. O., Wei, M. T., Stone, H. A. & Brangwynne, C. P. Quantifying dynamics in phase-separated condensates using fluorescence recovery after photobleaching. *Biophys. J.* **117**, 1285–1300 (2019).
35. Jawerth, L. et al. Protein condensates as aging Maxwell fluids. *Science* **370**, 1317–1323 (2020).
36. Patel, A. et al. A Liquid-to-solid phase transition of the ALS protein FUS accelerated by disease mutation. *Cell* **162**, 1066–1077 (2015).
37. Chen, W. et al. Endoskeletal coacervates with mobile-immobile duality for long-term utility. *Chem. Eng. J.* **462**, 142165 (2023).
38. van Brakel, J. & Heertjes, P. M. Capillary rise in porous media. *Nature* **254**, 585–586 (1975).
39. Yewdall, N. A., André, A. A. M., Lu, T. & Spruijt, E. Coacervates as models of membraneless organelles. *Curr. Opin. Colloid Interface Sci.* **52**, 101416 (2021).

40. de Kruif, C. G., Weinbreck, F. & de Vries, R. Complex coacervation of proteins and anionic polysaccharides. *Curr. Opin. Colloid Interface Sci.* **9**, 340–349 (2004).
41. Ye, S. et al. Micropolarity governs the structural organization of biomolecular condensates. *Nat. Chem. Biol.* **20**, 443–451 (2024).
42. Uthaman, A. et al. Characterization of nanoporous materials. In Advanced Functional Porous Materials; Springer Science and Business Media B.V. https://doi.org/10.1007/978-3-030-85397-6 (2022).
43. Feng, X. & Huang, R. Y. Liquid separation by membrane pervaporation: a review. *Ind. Eng. Chem. Res.* **36**, 1048–1066 (1997).
44. Capasso Palmiero, U. et al. Programmable zwitterionic droplets as biomolecular sorters and model of membraneless organelles. *Adv. Mater.* **34**, e2104837 (2022).
45. Schlenoff, J. B. Zwitteration: coating surfaces with zwitterionic functionality to reduce nonspecific adsorption. *Langmuir* **30**, 9625–9636 (2014).
46. Sponchioni, M., Rodrigues Bassam, P., Moscatelli, D., Arosio, P. & Capasso Palmiero, U. Biodegradable zwitterionic nanoparticles with tunable UCST-type phase separation under physiological conditions. *Nanoscale* **11**, 16582–16591 (2019).
47. Renaud de la Faverie, A., Guédin, A., Bedrat, A., Yatsunyk, L. A. & Mergny, J.-L. Thioflavin T as a fluorescence light-up probe for G4 formation. *Nucleic Acids Res.* **42**, e65–e72 (2014).
48. Driessen, R. P. C. et al. Effect of Temperature on the Intrinsic Flexibility of DNA and Its Interaction with Architectural Proteins. *Biochemistry* **53**, 6430–6438 (2014).
49. Olsen, C. M., Lee, H. T. & Marky, L. A. Unfolding Thermodynamics of Intramolecular G-Quadruplexes: Base Sequence Contributions of the Loops. *J. Phys. Chem. B* **113**, 2587–2595 (2009).
50. Riback, J. A. et al. Drummond, stress-triggered phase separation is an adaptive, evolutionarily tuned response. *Cell* **168**, 1028–1040 (2017).
51. Yu, M. & Nishiumi, H. Theory of phase separation in mixtures with lower critical solution temperature. *J. Phys. Chem.* **96**, 842–845 (1992).
52. Bohidar, H., Dubin, P. L., Majhi, P. R., Tribet, C. & Jaeger, W. Effects of protein-polyelectrolyte affinity and polyelectrolyte molecular weight on dynamic properties of bovine serum albumin-poly(-diallyldimethylammonium chloride) coacervates. *Biomacromolecules* **6**, 1573–1585 (2005).
53. Zhang, W. et al. Recent achievements in self-healing materials based on ionic liquids: A review. *J. Mater. Sci.* **55**, 13543–13558 (2020).
54. Cowburn, D. & Rout, M. Improving the hole picture: towards a consensus on the mechanism of nuclear transport. *Biochem. Soc. Trans.* **51**, 871–886 (2023).
55. Kamagata, K. et al. Characterization of design grammar of peptides for regulating liquid droplets and aggregates of FUS. *Sci. Rep.* **11**, 6643 (2021).
56. Chen, N., Lin, L., Sun, W. & Zhao, M. Stable and pH-sensitive protein nanogels made by self-assembly of heat denatured soy protein. *J. Agr. Food Chem.* **62**, 9553–9561 (2014).
57. Chen, N., Zhao, Z., Wang, Y. & Dimova, R. Resolving the mechanisms of soy glycinin self-coacervation and hollow-condensate formation. *ACS Macro Lett.* **9**, 1844–1852 (2020).

Acknowledgements

L. J. acknowledges support by National Natural Science Foundation of China (No. 22122201 and No. 21773092), Guangdong Basic and Applied Basic Research Foundation (No. 2023A1515010956), and The Recruitment Program of Guangdong (No. 2016ZT06C322). W. Z. acknowledges support from Guangdong Provincial Pearl River Talents Program (2019QN01Y314) and the Program for Guangdong Introducing Innovative and Entrepreneurial Teams (2019ZT08Y318).

Author contributions

H. W., W. Z., and L. J. conceived the project and designed the experiments. H. W., H. Z., W. T., and J. Z. performed the experiments. W. Z. provided facilities and help on the porous membranes. All the authors analyzed the data and contributed to discussing the results and writing the paper.

Competing interests

The authors declare no competing interests.

Additional information

Supplementary information The online version contains supplementary material available at https://doi.org/10.1038/s41467-024-54510-9.

Correspondence and requests for materials should be addressed to Wei Zhu or Lingxiang Jiang.

Peer review information *Nature Communications* thanks Andreas Dahlin, who co-reviewed with Jesper Medin and the other, anonymous, reviewers for their contribution to the peer review of this work. A peer review file is available.